Chaos, Solitons and Fractals 104 (2017) 228–237

Contents lists available at ScienceDirect

Chaos, Solitons and Fractals

Nonlinear Science, and Nonequilibrium and Complex Phenomena

journal homepage: www.elsevier.com/locate/chaos

Lyapunov analysis of the spatially discrete-continuous system dynamics

Vladimir A. Maximenko[a], Alexander E. Hramov[a,b], Alexey A. Koronovskii[b,*], Vladimir V. Makarov[a,b], Dmitry E. Postnov[b], Alexander G. Balanov[c]

[a] Yurij Gagarin State Technical University of Saratov, Politehnicheskaya, 77, Saratov 410054, Russia
[b] Saratov State University, Astrakhanskaya, 83, Saratov 410012, Russia
[c] Department of Physics, Loughborough University, Loughborough LE11 3TU, UK

ARTICLE INFO

Article history:
Received 21 May 2017
Revised 14 August 2017
Accepted 22 August 2017

Keywords:
Lyapunov exponents
Dynamical chaos
Spatially extended system
System with the small number of degrees of freedom
Numerical simulation
Microwaves
Reaction-diffusion model
Spreading depression

ABSTRACT

The spatially discrete-continuous dynamical systems, that are composed of a spatially extended medium coupled with a set of lumped elements, are frequently met in different fields, ranging from electronics to multicellular structures in living systems. Due to the natural heterogeneity of such systems, the calculation of Lyapunov exponents for them appears to be a challenging task, since the conventional techniques in this case often become unreliable and inaccurate. The paper suggests an effective approach to calculate Lyapunov exponents for discrete-continuous dynamical systems, which we test in stability analysis of two representative models from different fields. Namely, we consider a mathematical model of a 1D transferred electron device coupled with a lumped resonant circuit, and a phenomenological neuronal model of spreading depolarization, which involves 2D diffusive medium. We demonstrate that the method proposed is able reliably recognize regular, chaotic and hyperchaotic dynamics in the systems under study.

1. Introduction

It is quite common in complexity science, when a spatially extended media with infinitely many degrees of freedom interacts with a dynamical system localized in space and having a finite number of degrees of freedom. The mathematical models of such discrete-continuous systems (DCS) are composed of partial differential equations (PDEs) coupled with ordinary differential equations (ODEs).

The models that fall to the class of discrete-continuous systems arise in many applications from different research fields ranging from life sciences to information processing and electronics. Incomplete list of such problems includes modeling of drug delivery to biological tissues [1], neural dynamics [2], mitochondrial swelling [3], intracellular signaling [4], cortical spreading depression [5], quantum information processing [6], active semiconductor media interacting with discrete elements [7], lumped circuits coupled to a transmission line [8], multiscale continuum mechanics [9].

The similar class of model systems appears in the number of biophysical problems, where the hemodynamics, which is often described by Navier–Stokes PDEs, is considered together with the time-variable system-wide quantities, e.g., the blood pressure or electrocardiography (ECG) [10,11].

Due to the importance of the spatially discrete-continuous models for the different research fields, the specialized solution algorithms were developed (e.g. [12]). However, there is a clear shortfall of the tools available for stability analysis of such dynamical systems. DCSs are often analysed with the help of methods, developed for systems with finite number of the degrees of freedom. In this context the original spatially-distributed subsystem can be described by the set of ODEs based on lattice model [13] or Laplace transform method [14]. In electronics the dynamics of DCSs are often analysed by the consideration of the subsystems with finite number of the degrees of freedom and spatially-extended subsystem separately [15,16]. These approaches, obviously, have their specific limitations. In particular, transition to the lattice model can potentially affects the system dynamics in an unpredictable way [13], while the consideration of the dynamical regimes taking place in finite-dimensional subsystem may not reflect the key features of spatiotemporal behaviour of spatially extended subsystem [17].

* Corresponding author.
E-mail address: alexey.koronovskii@gmail.com (V.A. Maximenko).

http://dx.doi.org/10.1016/j.chaos.2017.08.021
0960-0779/

The most promising approach for the stability analysis of DCSs is based on the calculation of Lyapunov exponents (LEs). The use of such tool makes the significant progress in study of the finite-dimensional flow systems [18,19], discrete maps [20] and time-series [21] (including the cases with the presence of noise, see, e.g, [22]). In recent works Lyapunov exponents are applied for analysis of non Hermitian Hamiltonian systems [23] and neural systems [24]. In the case of spatiotemporal dynamics the calculation of LEs is more complicated [25,26]. At the same time, the recent results on Lyapunov analysis of the extended media, described within the framework of hydrodynamic approximation has shown a great potential of this technique for the quantitative assessment of chaotic behavior [26,27], detection of hyper-chaotic regimes [28] and identification of the synchronous modes in coupled spatially extended elements [28] as well as networks of interacting spatially extended units [29,30].

It should be noted, the existent methods of the LEs calculation either for the finite-dimensional systems [31] (such as flows or maps) or spatially extended media [28] cannot be directly applied to DCSs, i.e., to the systems consisting of both the spatially extended and concentrated in space subsystems. The main problem here is that the reference states of such systems are determined simultaneously by two significantly different types of variables, namely, by the variables depending only on time (which correspond to the finite dimensional subsystems) and by the functions which depend both on time and space coordinates (they represent the spatially extended subsystems). This makes impossible the straightforward implementation of the normalization and orthogonalization procedures, developed for the finite dimensional [31] and spatially-extended [28] systems and, as the results, the accurate estimation of Lyapunov exponents.

In the present paper we introduce an approach allowing to calculate the spectrum of LEs for discrete-continuous dynamical systems. In order to illustrate the universality and capability of the proposed method as well as its relevance, we apply the developed approach to analyze the stability of dynamical regimes in two radically different exemplary DCS that came from different research fields.

First, we perform the Lyapunov stability analysis of the charge dynamics in a finite-dimensional dynamical circuit, where a spatially extended 1D media is included as an nonlinear element [7]. The latter is described by a set of the coupled Poisson and continuity equations, whereas the circuit is described with the help of non-stationary Kirchhoff equations.

Next, we consider an example from different research area. Namely, we analyze the dynamics of a phenomenological model of spreading depolarization [5], that is composed of a set of FitzHugh–Nagumo (FHN) oscillators (model neurons) coupled through 2D diffusive media that describe the extracellular spreading of depolarizing substances.

In both cases the Lyapunov analysis allowed us to reveal and quantify the transitions between the regular and chaotic dynamics with variation of the control parameters.

The paper has the following structure. The approach to calculation of the spectrum of LEs for DCS is described in Section 2. The dynamics of the RLC-circuit connected with the semiconductor transferred electron device (TED) is described and analyzed in Section 3. Section 4 is devoted to the Lyapunov stability analysis of the model of the spreading depolarization. The final remarks and conclusions are given in Section 5.

2. Calculation of the Lyapunov exponents for spatially discrete-continuous systems

Let us consider an arbitrary DCS, which is described by a set of coupled PDEs and ODEs. The state of the spatially extended medium modeled by PDEs is supposed to be defined by N variables, each being a function of both the displacement vector $\mathbf{r}$ and time t

$$\Phi_1(\mathbf{r},t),\Phi_2(\mathbf{r},t),\ldots,\Phi_{N-1}(\mathbf{r},t),\Phi_N(\mathbf{r},t),\quad \mathbf{r}\in\mathbb{R}^D,\quad 0\le t\le\infty, \tag{1}$$

D is the dimension of the space (in our study $D=1$ for the system considered in Section 3 and $D=2$ for the discrete-continuous model of the spreading depression discussed in Section 4). The variables depending only on time

$$\Theta_1(t),\Theta_2(t),\ldots,\Theta_{M-1}(t),\Theta_M(t),\quad 0\le t\le\infty. \tag{2}$$

describe the state of the subsystems with $M/2$ degrees of freedom defined by ODEs.

In order to characterize the stability of the DSC dynamics, one has to trace the evolutions of the system state (in our case it is $\mathbf{U}(\mathbf{r},t)=(\Phi_1(\mathbf{r},t),\ldots,\Phi_N(\mathbf{r},t),\Theta_1(t),\ldots\Theta_M(t))^T$) and analyse how a linear perturbation of this state changes with time. However, this procedure for the case when state variables depend only on time [31,32] is significantly different from the case, when the state variables depend both on time and displacement [27,28]. In our situation we deal with a mix of two type of the variables mentioned above, which prevents a direct application of the convention routines. To overcome this conceptual obstacle, we propose to consider the variables (2) as the spatially extended ones, i.e.,

$$\Psi_k(\mathbf{r},t)=\Theta_k(t),\quad k=\overline{1,M}. \tag{3}$$

In this case the state of the spatially discrete-continuous system may be considered as

$$\mathbf{U}(\mathbf{r},t)=(\Phi_1(\mathbf{r},t),\ldots,\Phi_N(\mathbf{r},t),\Psi_1(\mathbf{r},t),\ldots,\Psi_M(\mathbf{r},t))^T, \tag{4}$$

and the evolution operator

$$\hat{L}(\mathbf{U}(\mathbf{r},t)), \tag{5}$$

determines the spatiotemporal behavior of the system state. This evolution operator consists typically of coupled ordinary differential equations and partial differential equations determining the evolution of localized in space subsystems and spatially extended media, respectively. E.g., for the RLC-TED circuit considered in Section 3 the evolution operator (5) consists of ODEs (19) and PDEs (20)–(21) with the boundary conditions (24). Assume that $\mathbf{r}=x$ in the case of $D=1$, $\mathbf{r}=(x,y)$ when $D=2$ and $\mathbf{r}=(x,y,z)$ for $D=3$.

The numerical algorithms for the LE calculation are usually based on the analysis of the perturbation $\mathbf{V}(\mathbf{r},t)$ of the reference state $\mathbf{U}(\mathbf{r},t)$ and the calculation of the increment/decay rate. To estimate the K largest Lyapunov exponents Λ_i, $i=1,\ldots,K$, one has to consider a set of orthogonal perturbations $\mathbf{V}_i(\mathbf{r},t), i=1,\ldots,K$. In this case, the Lyapunov exponents characterize the exponential growth/decay of K orthogonal modes of $\mathbf{U}(\mathbf{r},t)$. Each perturbation $\mathbf{V}_i(\mathbf{r},t)$ is defined as

$$\mathbf{V}_i(\mathbf{r},t)=(\tilde{\phi}_1^i(\mathbf{r},t),\ldots,\tilde{\phi}_N^i(\mathbf{r},t),\tilde{\psi}_1^i(\mathbf{r},t),\ldots,\tilde{\psi}_M^i(\mathbf{r},t))^T,\quad i=\overline{1,K} \tag{6}$$

assuming that all $\tilde{\psi}_k^i(\mathbf{r},t)$ depend only on time, i.e.,

$$\tilde{\psi}_k^i(\mathbf{r},t)\equiv\tilde{\theta}_k^i(t),\quad \forall k,\ \forall i. \tag{7}$$

The perturbations introduced must initially be orthogonal and normalized. The orthogonality condition reads

$$(\mathbf{V}_i(\mathbf{r},0),\mathbf{V}_j(\mathbf{r},0))=\begin{cases}1, i=j,\\ 0, i\ne j.\end{cases} \tag{8}$$

where the brackets $(\cdot,\cdot)$ denote the scalar product

$$(\mathbf{V}_i(\mathbf{r},t),\mathbf{V}_j(\mathbf{r},t)) = \begin{cases} \int_L \left(\sum_{l=1}^{N} \tilde{\phi}_l^i(x,t)\tilde{\phi}_l^j(x,t)\right) dx + \\ + \int_L \left(\sum_{l=1}^{M} \tilde{\psi}_l^i(x,t)\tilde{\psi}_l^j(x,t)\right) dx, & \text{if} \quad D=1, \\ \iint_S \left(\sum_{l=1}^{N} \tilde{\phi}_l^i(x,y,t)\tilde{\phi}_l^j(x,y,t)\right) dx\,dy + \\ + \iint_S \left(\sum_{l=1}^{M} \tilde{\psi}_l^i(x,y,t)\tilde{\psi}_l^j(x,y,t)\right) dx\,dy, & \text{if} \quad D=2. \end{cases} \tag{9}$$

Due to Eq. (7) the integral of the second term in Eq. (9) is

$$\int_L \left(\sum_{l=1}^{M} \tilde{\psi}_l^i(\mathbf{r},t)\tilde{\psi}_l^j(\mathbf{r},t)\right) d\mathbf{r} = L \times \sum_{l=1}^{M} \tilde{\theta}_l^i(t)\tilde{\theta}_l^j(t), \tag{10}$$

and, therefore, Eq. (9) may be considered as the sum of the weighed Euclidean scalar product for the discrete part and the scalar product for the continuous part of the state space.

The normalization means that

$$||\mathbf{V}_i(\mathbf{r},t_r)|| = 1, \tag{11}$$

where $||\mathbf{V}_i|| = \sqrt{(\mathbf{V}_i,\mathbf{V}_i)}$, and t_r are the time moment, when the normalization is required. The set of the perturbations $\mathbf{V}_i(\mathbf{r},t)$, $i = \overline{1,K}$, which fulfill the requirements of Eqs. (8) and (11) at $t = t_r$ can be built with the help of the Gram-Schmidt procedure

$$\hat{\mathbf{V}}_1(\mathbf{r},t_r) = \varphi_1(\mathbf{r}) \tag{12}$$

$$\hat{\mathbf{V}}_{i+1}(\mathbf{r},t_r) = \varphi_{i+1}(\mathbf{r}) - \sum_{k=1}^{i} (\mathbf{V}_k(\mathbf{r},t_r),\varphi_{i+1}(\mathbf{r}))\mathbf{V}_k(\mathbf{r},t_r) \tag{13}$$

$$i = 1,2,\ldots,K-1;$$

$$\mathbf{V}_i(\mathbf{r},t_r) = \frac{\hat{\mathbf{V}}_i(\mathbf{r},t_r)}{||\hat{\mathbf{V}}_i(\mathbf{r},t_r)||}$$

$$i = 1,2,\ldots,K. \tag{14}$$

Here $\hat{\mathbf{V}}_1(\mathbf{r},t_r)$, $\hat{\mathbf{V}}_2(\mathbf{r},t_r),\ldots,\hat{\mathbf{V}}_K(\mathbf{r},t_r)$ generate a system of orthogonal vectors, while $\varphi_1(\mathbf{r})$, $\varphi_2(\mathbf{r})$, ..., $\varphi_K(\mathbf{r})$ are the auxiliary functions, which are chosen arbitrary for the initial moment of time.

The evolution of the perturbations is described by the operator (5) linearized in the vicinity of the reference state

$$\partial\hat{L}(\mathbf{U}(\mathbf{r},t),\mathbf{V}_i(\mathbf{r},t)). \tag{15}$$

Again, the linearized evolution operator (15) should be obtained with the help of the linearization of the ODEs and PDEs being the constituent subunits of the initial evolution operator (5).

In order to find the LEs spectrum, one needs to follow the time evolution of both the reference state $\mathbf{U}(\mathbf{r},t)$ and its perturbations $\mathbf{V}_i(\mathbf{r},t)$ $(i = 1,2,\ldots,K)$ by the self-consistent integration of Eqs. (5) and (15). With this, the Gram-Schmidt procedure (12)–(14) should be periodically applied over a certain time period Γ (see Ref. [32]) at time moment $t_r = j\Gamma$ $(j = 1,\ldots,I)$ with newly defined set of functions

$$\varphi_i(\mathbf{r}) = \mathbf{V}_i(\mathbf{r},t_r). \tag{16}$$

After the sufficiently large number, I, of such repetitions the perturbations $\mathbf{V}_i(\mathbf{r},t_r)$ taken after orthogonalization (Eqs. (12) and (13)) but before renormalization (Eq. (14)) are used to find Lyapunov sums

$$S_i = \sum_{j=1}^{I} \ln||\hat{\mathbf{V}}_i(\mathbf{r},j\Gamma)||, \tag{17}$$

which yields LEs as

$$\Lambda_i = \frac{S_i}{I\Gamma}. \tag{18}$$

Summarizing the formalism given above, Lyapunov exponents for spatially discrete-continious dynamical systems can be calculated using the following algorithm:

1. determination of the system reference state $\mathbf{U}(\mathbf{r},t)$ in form given be Eq. (4), where the set of variables $\Theta_k(t)$ (see Eq. (2)) uniquely describes the state of the subsystem with the finite number of degrees of freedom and variables $\Phi_k(\mathbf{r},t)$ (1) describe the state of the spatially-extended subsystem;
2. determination of the small perturbations $\mathbf{V}_i(\mathbf{r},t)$ of the system state in the form of Eq. (6);
3. obtaining equations, which describe the spatio-temporal evolution of the small perturbations, $\mathbf{V}_i(\mathbf{r},t)$, by the linearization of the equations (in the vicinity of the reference state, $\mathbf{U}(\mathbf{r},t)$), describing the system state evolution;
4. realization of Gram–Schmidt procedure (12) – (14) for generating a system of orthogonal perturbations $\mathbf{V}_i(\mathbf{r},t)$ with $|\mathbf{V}_i(\mathbf{r},t)| = 1.0$;
5. implementation of the algorithms for numerical simulation of the evolution of system state $\mathbf{U}(\mathbf{r},t)$ with the set of perturbations $\mathbf{V}_i(\mathbf{r},t)$;
6. sequential repetition of steps 4 and 5 with Lyapunov sums (17) calculation;
7. Lyapunov exponents calculation according to Eq. (18).

This algorithm can be applied to the mathematical models from different fields of science. In the next sections of the paper we apply the proposed algorithm to fundamentally different DCSs, namely, the electronic (Section 3) and neural (Section 4) systems, for which the reference system state $\mathbf{U}(\mathbf{r},t)$ is described by the set of variables, part of which depend on time, while others depend on time and spatial coordinate.

3. Chaos in RLC-TED circuit

First, we have applied the proposed approach to a practical example of electronic systems (a two-terminal transferred electron device (TED) coupled with a RLC-circuit). Here, the TED plays a the role of a 1D nonlinear active medium, while the RLC-circuit is a dynamical system with a finite number of degrees of freedom. Fig. 1 a,b present the equivalent electric circuit of this device, where TED is represented by a nonlinear resistor (Fig. 1 b). The time-depended current through this resistor $I(V_{TED})$ is generated in response to the voltage V_{TED} applied across two terminals of the TED. Variables V_1 and I_1 are the voltage drop across the capacitor and the current through the inductor, respectively, $R = 17\ \Omega$ is the resistance of the circuit. The values of the capacitance C and the inductance L are the adjustable parameters of the circuit, V_0 is the dc bias, which we use as the main control parameter of the model under study.

3.1. Model

The circuit in Fig. 1 a,b can be described by ODEs based on the Kirchhoff rules.

$$\frac{dV_1}{dt} = \frac{I(V_{TED}) - I_1}{C},$$
$$\frac{dI_1}{dt} = \frac{V_1 - RI_1}{L},$$
$$V_{TED} = V_0 - V_1. \tag{19}$$

From physical point of view Eq. (19) can be understood as a mathematical model of a TED interacting with an external

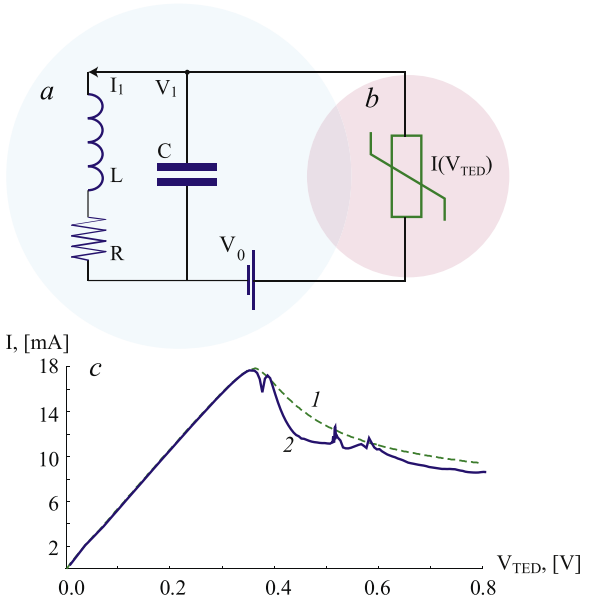

Fig. 1. (*a*) The equivalent circuit of the finite-dimensional system represented by the RLC-circuit coupled with (*b*) the spatially extended active element represented by the transferred electron device. $I_1(t)$ and $V_1(t)$ are the current and the voltage in the circuit. (*c*) The current-voltage characteristic of this element without (curve 1) and with (curve 2) external circuit. The control parameters of the circuit are $f_Q = 13.81$ GHz,Q=150.

single-mode resonator, whose the eigenfrequency f_Q and the quality factor Q are determined as $f_Q = 1/(2\pi\sqrt{LC})$ and $Q = (1/R)\sqrt{L/C}$, respectively.

We consider realistic circuit parameters evaluated from the recent experiments with superlattice coupled with a resonant circuit [7].

As a mathematical model of TED we consider the self-consistent system of the one-dimensional current continuity and the Poisson equation, which are used widely to describe charge transport processes in solid state and plasma physics, including Pierce beam-plasma system [33], non-neutral plasma [34], simple plasma diodes [35,36], semiconductors [37,38], organic field-effect transistors [39], etc. Such model was shown to demonstrate a variety of nonlinear phenomena including developing instabilities of electron transport in Pierce diode [40] and semiconductor structures [37], developing of turbulence [41] and bifurcations in plasma drift waves [42,43].

As an example of a TED we consider a miniband semiconductor superlattice which has been proposed in works [44,45] and has became a classical model for analysis of nonlinear phenomena of charge transport [46]. For this type of TED the model equations have a form

$$\frac{\partial n}{\partial t} = -\frac{1}{e}\frac{\partial J}{\partial x}, \tag{20}$$

$$\frac{\partial F}{\partial x} = \frac{e}{\epsilon_0\epsilon_r}(n - n_0), \tag{21}$$

where $e > 0$ is the absolute value of electron charge, n and J are charge and current densities, respectively, and F is an electric field strength. The values of relative permittivitie $\epsilon_r = 12$ and the equilibrium volume density of charge carriers $n_0 = 3 \times 10^{22}$ m^{-3} correspond to realistic devices [47,48]. The current density is estimated as

$$J(x,t) = en(x,t)v_d(F(x,t)), \tag{22}$$

and the drift velocity is calculated using the Esaki–Tsu formula [44]

$$v_d(F(x,t)) = \alpha\frac{\beta F(x,t)}{1 + (\beta F(x,t))^2}. \tag{23}$$

For our model we define $\alpha = 5.6 \times 10^4$ m/s and $\beta = 3.15 \times 10^{-6}$ mV^{-1}. The voltage $V_{TED}(t)$ dropped along the TED device of length $\mathcal{L} = 100$ nm determines the boundary condition

$$V_{TED}(t) = \int_0^{\mathcal{L}} F(x,t)\,dx. \tag{24}$$

Fig. 1, *c* shows the current voltage characteristics of the autonomous superlattice (dashed curve 1), when V_{TED} is constant, and for the case, when superlattice is coupled with the resonant circuit (solid curve 2). They were calculated by averaging the stationary (taken after some relaxation) current $I(t)$ over time. In the case of the autonomous superlattice the current-voltage characteristic demonstrates a rise-and-fall shape, where the descending part of the curve is associated with appearance of periodic current self-oscillations caused by traveling charge domains [38]. Coupling to the resonant circuit significantly modifies this part of the current-voltage characteristics by generation of a series of additional peaks. Previously it was shown that these features relate to the development of additional instabilities in the system, which can lead to emergence of chaos [7,49].

3.2. Lyapunov analysis

According to step 1 of the algorithm (see. Section 2), the state of the model considered in Section 3.1 can be defined by a vector

$$\mathbf{U}(x,t) = (n(x,t), I(x,t), V(x,t))^T, \tag{25}$$

where component $n(x, t)$ unambiguously determines the state of the medium (20)–(22) [27,28], and variables $I(x,t) = I_1(t), V(x,t) = V_1(t), \forall x \in [0, \mathcal{L}]$ characterize the state of the RLC-circuit.

To calculate the spectrum of K highest Lyapunov exponents, in agreement with step 2 of the algorithm we use the set of the small perturbations

$$\mathbf{V}_i(x,t) = (\tilde{n}_i(x,t), \tilde{I}_i(x,t), \tilde{V}_i(x,t))^T, i = \overline{1,K}. \tag{26}$$

According to the step 3 of the algorithm (see. Section 2) time evolution of the introduced perturbations is govern by the linear operator (15), which is defined by a set of linear ODEs

$$\begin{aligned}
\frac{d\tilde{V}_i}{dt} &= \frac{\tilde{I}(\tilde{V}_{TED}) - \tilde{I}_i}{C}\\
\frac{d\tilde{I}_i}{dt} &= \frac{\tilde{V}_i - R\tilde{I}_i}{L}\\
\tilde{V}_{TED} &= -\tilde{V}_i
\end{aligned} \tag{27}$$

and PDEs

$$\begin{aligned}
\frac{\partial\tilde{n}_i}{\partial t} &= -\frac{1}{e}\frac{\partial\tilde{J}_i}{\partial x}\\
\frac{\partial\tilde{F}_i}{\partial x} &= \frac{e}{\epsilon_0\epsilon_r}(\tilde{n}_i)\\
\tilde{J}_i &= e\tilde{n}_i v_d(F) + en\frac{dv_d(F)}{dF}\tilde{F}_i
\end{aligned}$$

$$\int_0^{\mathcal{L}} \tilde{F}_i\,dx = \tilde{V}_{TED}, \tag{28}$$

derived by linearization of Eqs. (19)–(24).

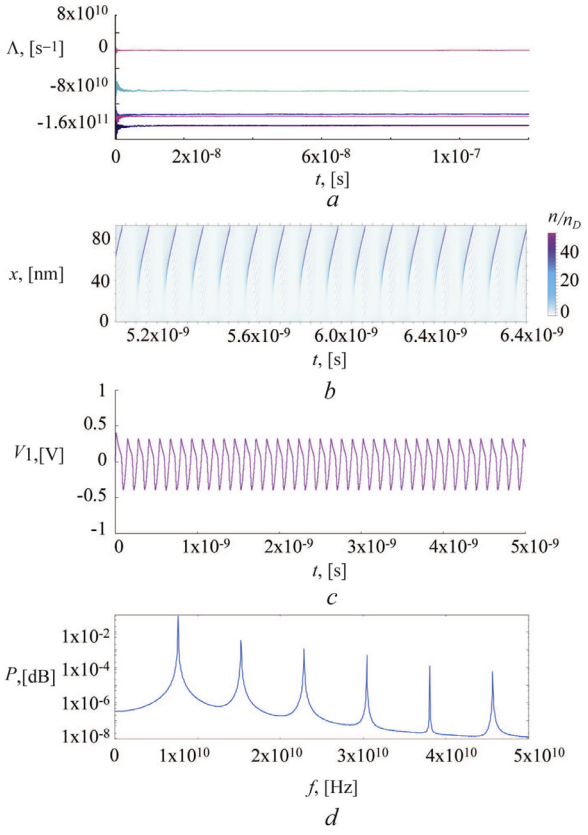

Fig. 2. The spectrum of five highest LEs (*a*), the spatiotemporal dynamics of the reference state of the extended subsystem (*b*), the dynamics of the voltage in the circuit (*c*) and the power spectrum of the voltage oscillations (*d*), corresponded to the periodical regime, obtained for the spatially extended device interacting with the external circuit for $V_0 = 0.45$ V.

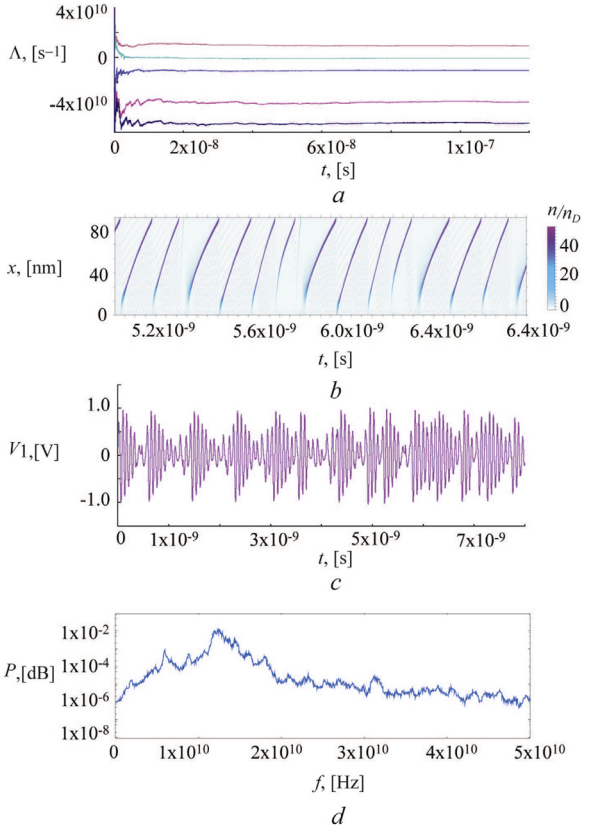

Fig. 3. The spectrum of five highest LEs (*a*), the spatiotemporal dynamics of the reference state of the extended subsystem (*b*), the dynamics of the voltage in the circuit (*c*) and the power spectrum of the voltage oscillations (*d*), corresponded to the chaotic regime, obtained for the spatially extended device interacting with the external circuit for $V_0 = 0.86$ V.

The set of perturbations (26) has been obtained with the help of Gram–Schmidt procedure (step 4). Following step 5 of the algorithm (see. Section 2) we have applied the numerical simulation of the Eqs. (19)–(24) which describe evolution of system state with Eqs. (27)–(28) describing the development of small perturbations.

First, to demonstrate the effectiveness of the proposed technique, we consider the charge dynamics in the system for two representative values of V_0, namely $V_0 = 0.45$ V and $V_0 = 0.86$ V.

The results of numerical calculations for $V_0 = 0.45$ V are presented in Fig. 2. Fig. 2, *a* displays the dependencies of the five largest LEs on time, illustrating the convergence of the method. For this dependence the exponents were calculated (steps 6 and 7) using Eq. (18) for different time intervals $t = I\Gamma$, where $I = 1, 2, \ldots$ and $\Gamma = 125$ fs. Being unstable for small t, after $t \approx 20$ ns the values of the LEs are stabilized with the largest exponent approximately equal to zero, which predicts a periodic character of charge dynamics for the given V_0. To verify this, we plot realisation of the medium state variable $n(x, t)$ (Fig. 2, *b*) and the variable $V_1(t)$ characterizing the circuit (Fig. 2, *c*). One can see that the charge redistribution in the TED is associated with periodically travelling charge domains (areas of high concentration of charge), which cause regular oscillations of the voltage drop V_1(t). These oscillations are characterised by a discrete spectrum consisting of a number of harmonics (Fig. 2, *d*). Thus, the periodic behaviour predicted by the calculations of the Lyapunov exponents is completely confirmed by analysis of the dynamical patterns in the system.

The behaviour of the LEs changes for $V_0 = 0.86$ V. Now, convergence of the Lyapunov exponents takes a longer time, $t \approx 60$ ns (compare Figs. 3, *a* and 2, *a*). After the transient time the largest LE has the positive value, while the second largest exponent converges to zero. Such spectrum of the exponents indicates the presence of chaotic dynamics. This fact is reflected in irregular pattern in spatio-temporal dynamics of charge along SL displayed in Fig. 3, *b*, and in aperiodic character of $V_1(t)$ oscillations presented in Fig. 3, *c*. The continuous spectrum of these oscillations (see Fig. 3, *d*) provides an additional evidence of chaos developed of the system.

Thus, the method is shown to be is able to distinguish regular and chaotic dynamics in the model under study. The calculations of LEs performed for a wide range of different values V_0 revealed that a reliable estimation of LEs requires minimum $I = 10^6$ Gram–Schmidt iterations. Therefore, this number I is used in our further analysis.

Next, we study how variation of the bias voltage V_0 and the resonant frequency of the RLC- circuit f_Q affects the stability of the system. The dependencies of four largest LEs on V_0 for fixed $f_Q =$ 13.81 GHz (selected according to the experimental work [7]) are shown in Fig. 4, *a*.

For low $V_0 < 0.35$ V, all LEs have negative values, revealing the equilibrium state in the system. With increase V_0 the largest LE becomes zero indicating a transition to periodic dynamics. Further growth of V_0 leads to appearance of a positive LE at $V_0 =$ 0.504 V, which corresponds to onset a chaos is the system. This chaotic regimes is changed by periodic dynamics at $V_0 = 0.521$ V. In general, within the bias voltage range 0–0.8 V the Lyapunov analysis reveals few regions of chaos highlighted by grey shadow in Fig. 4, *a*. One can see that the appearance of the chaotic regimes corresponds to the occurrence of additional peaks in the

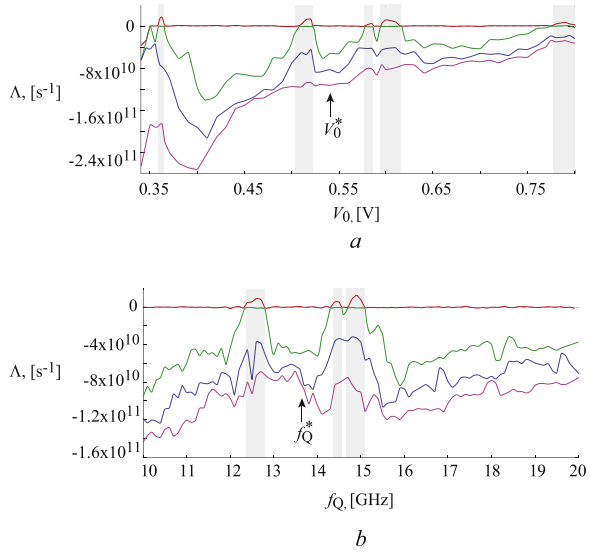

Fig. 4. The dependencies of four highest LEs on the supply voltage V_0 ($f_Q^* = 13.7$ GHz) (*a*) and the eigenfrequency f_Q ($V_0^* = 0.54$ V). (*b*) The areas of chaotic dynamics are shown by grey shadow.

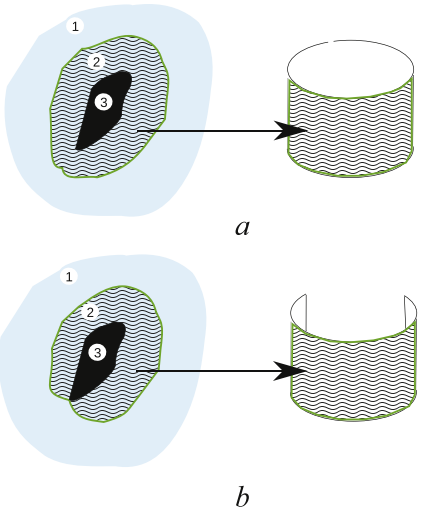

Fig. 5. On the boundary conditions for model (29)-(30). Left: schematic drawing of healthy (1), injured (3), and susceptible to depolarization wave area (2) (penumbra). Right: spatial configuration of the model. Closed or non-closed area (2) is modeled with periodic (a) or non-periodic (b) boundary conditions.

current-voltage characteristic (solid curve in Fig. 1, *c*). Fig. 4, *b* shows four largest LE in dependence on f_Q, changing between 10 and 20 GHz. Although the dominant dynamics is periodic, i.e characterised by zero largest LE, the graphs reveal the regions of chaos, where the largest LE becomes positive. Thus, this analysis shows that either changes V_0 or f_Q can induce the chaotic dynamics in the system, which potentially can be used in practical applications [50].

4. Spreading depolarization model

Here, we apply our method to more complex DCS, where a number of discrete components are spread across a 2D continuous medium. As an example we consider a simplified model, which describes dynamical mechanisms underlying the extreme physiological behaviors in brain cortex, such as spreading depression [51], migraine waves [52], and peri-infarct depolarization waves [53].

The essential feature of listed phenomena is the drastic changes in neuron activity, supported by the massive redistribution of ions in extracellular space, so called “volume transmission” [54]. The later, speaking in physical terms, is provided by the diffusion in porous medium. While this diffusion process by its nature falls to the class of continuous-media problems, the pattern of neuronal activity is formed by the discrete set of cells, each possesses their own dynamics. Thus, one arrive to specific form of DCS model, where the discrete set of active units is embedded in continuous medium.

4.1. Model equations

At a very simple level, a population of neurons coupled via the extracellular space can be modeled by means of one-component reaction-diffusion system connected with the discrete set of excitable units [13,55]. The former describes the spatial spreading of depolarization substances (potassium, glutamate) in extracellular space, while the later stands for the activity of neuronal population. In [55], such a model was implemented with a set of FitzHugh–Nagumo (FHN) model neurons, that are placed in the nodes of 2D space grid, and coupled with each other through the continuous diffusive medium. Each model neuron is assumed to be located at specific point $\mathbf{r}_{ij} = (x_i, y_j)$, $x_i = ih_x$, $y_j = jh_y$ and its dynamics is described by the ordinary differential equations

$$\begin{aligned} \varepsilon_v \frac{dv_{ij}(t)}{dt} &= v_{ij}(t) - v_{ij}^3(t)/3 - w_{ij}(t) + z(x_i, y_j, t), \\ \tau_l \frac{dw_{ij}(t)}{dt} &= A + Bv_{ij}(t) - w_{ij}(t), \end{aligned} \tag{29}$$

where $v_{ij}(t)$ and $w_{ij}(t)$ are the voltage variable and its recovery variable, respectively. These variables describe the state of each cell. The function $z(x, y, t)$ is defined on two-dimensional space $\mathbf{r} = (x, y)$ and describe the temporal changes of extracellular concentrations of depolarizing substances,which are supposed to be spreading in space [5]. Therefore, the dynamics of z is described by the partial differential equation:

$$\varepsilon_z \frac{\partial z}{\partial t} = \alpha_z \Psi(v) - z + \gamma \left(\frac{\partial^2 z}{\partial x^2} + \frac{\partial^2 z}{\partial y^2} \right), \tag{30}$$

where

$$\Psi(v) = \frac{1}{2}\left(1 + \tanh\left(\frac{v}{v_s}\right)\right) \tag{31}$$

is a sigmoid function that depends on v: at small v_s it approaches zero for $v < 0$, and unity for $v > 0$ (see Ref. [55] for details). In spatial domain, at the points $\mathbf{r}_{ij}$ occupied by model neurons, variable v, is supposed to be equal to the voltage variable v_{ij} of specific model neuro unit and (31) is applied, while in all other spatial locations $\Psi(v)$ was set to zero (no influx to the extracellular space).

The boundary conditions for z depend on specific problem under consideration. The peri-infarct depolarization waves (PIDs) are typically observed in the form of re-entrant waves circulating in closed area that surrounds the injured tissue but in turn is bounded by the healthy one (Fig. 5). At a very basic level, such environment can be modeled with a rectangular space with mixed boundary conditions (b.c.). Specifically, the boundary for y coordinate was composed from the Neumann b.c. and Dirichlet b.c. This combination was previously shown to trigger the autonomous pacemaker [5]. The boundary condition for x was periodic, so the left edge of simulated area was connected to the right edge, as shown in the Fig. 5 a. However, the diffusion rate at this junction line was assumed to be adjustable down to zero. The later extreme case actually provided the diconnected left and right egdes (each with Neumann b.c.), as shown in Fig. 5 b.

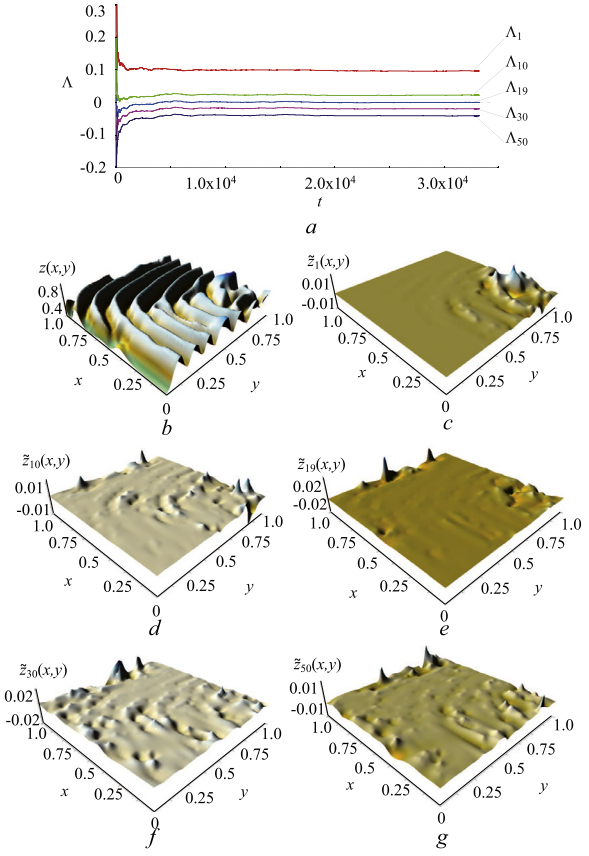

Fig. 6. The spectrum of Lyapunov exponents for the CSD model, containing the 1st and the 10th positive LEs, 19th LE (zero Lyapunov exponent), 30th and 50th negative LEs (*a*), 2-D distribution of the spatially extended variable $z(x, y, t)$ (*b*) and its perturbations (*c* – *g*), corresponded, respectively, to the presented LEs.

Computationally, the above described adjustment of boundary conditions was implemented by means of scale factor k_d as follows:

$$\varepsilon_z \frac{dz_{1,j}}{dt} = \alpha_z \Psi(v_{1,j}) - z_{1,j} + \gamma(z_{2,j} - z_{1,j}) + k_d \gamma(z_{N,j} - z_{1,j}), \tag{32}$$

$$\varepsilon_z \frac{dz_{N,j}}{dt} = \alpha_z \Psi(v_{N,j}) - z_{N,j} + \gamma(z_{N-1,j} - z_{N,j}) + k_d \gamma(z_{1,j} - z_{N,j}). \tag{33}$$

In (32),(33) $z_{1,j}$ and $z_{N,j}$, with $j = 1 \ldots N$ refer to left and right edges of $N \times N$ lattice that approximates the modeled medium. With this, if $k_d = 1$ then left and right edges of model space are connected like any other locations, while for $k_d = 0$ left and right edges become disconnected. Below we adjust k_d parameter only, while all other control parameters of the system (29)–(30) were set according to the previous work [5] as follows: $A = 0.5$, $B = 1.1$, $\tau_l = 1.0$, $\varepsilon_z = 1.0$, $\alpha_z = 1.1$, $\varepsilon_v = 0.004$, $\gamma = 7.5 \times 10^{-4}$, $v_s = 0.05$, $h_x = h_y = h = 0.025$.

For the chosen set of the control parameters and $k_d = 1$ the system demonstrate the complex wave pattern (Fig. 6, *b*) that consists of two distinctive areas, one being the nucleation center (right corner in the figure panel), and the other is filled with propagating waves. In order to classify this type of the behavior and to characterize it quantitatively, we apply the developed technique of Lyapunov exponent calculation.

4.2. Lyapunov exponents

Following the algorithm, given in Section 2 (see step 1), the reference state of the spreading depolarization model was chosen as

$$\mathbf{U}(x,y,t) = (V_{11}(x,y,t), W_{11}(x,y,t), V_{12}(x,y,t), W_{12}(x,y,t), \ldots, V_{ij}(x,y,t), W_{ij}(x,y,t), \ldots, V_{NN}(x,y,t), W_{NN}(x,y,t), z(x,y,t))^T, \tag{34}$$

where $V_{ij}(x,y,t) = v_{ij}(t)$ and $W_{ij}(x,y,t) = w_{ij}(t)$, N^2 is the number of the FHN oscillators. The scalar product of these states was calculated via Eq. (9), where the integration was performed over both x and y ranges.

According to step 2, the perturbation of the system state was written in form

$$\mathbf{V}(x,y,t) = (\tilde{V}_{11}(x,y,t), \tilde{W}_{11}(x,y,t), \tilde{V}_{12}(x,y,t), \tilde{W}_{12}(x,y,t), \ldots, \tilde{V}_{ij}(x,y,t), \tilde{W}_{ij}(x,y,t), \ldots, \tilde{V}_{NN}(x,y,t), \tilde{W}_{NN}(x,y,t), \tilde{z}(x,y,t))^T, \tag{35}$$

In order to describe the evolution of the perturbations, $\tilde{V}_{ij}(x,y,t)$, $\tilde{W}_{ij}(x,y,t)$ and $\tilde{z}(x,y,t)$ (step 3) the linear operator was obtained by the linearizion of Eq. (30) in the vicinity of the reference state as

$$\begin{aligned}
\varepsilon_v \frac{\partial \tilde{V}_{ij}(x,y,t)}{\partial t} &= \tilde{V}_{ij}(x_i,y_j,t) - V_{ij}^2(x_i,y_j,t)\tilde{V}_{ij}(x_i,y_j,t) \\
&\quad -\tilde{W}_{ij}(x_i,y_j,t) + \tilde{z}(x_i,y_j,t), \\
\tau_l \frac{\partial \tilde{W}_{ij}(x,y,t)}{\partial t} &= B\tilde{V}_{ij}(x_i,y_j,t) - \tilde{W}_{ij}(x_i,y_j,t), \\
\varepsilon_z \frac{\partial \tilde{z}(x,y,t)}{\partial t} &= \alpha_z \Phi(v)\tilde{v} - \tilde{z}(x,y,t) \\
&\quad +\gamma\left(\frac{\partial^2 \tilde{z}(x,y,t)}{\partial x^2} + \frac{\partial^2 \tilde{z}(x,y,t)}{\partial y^2}\right),
\end{aligned} \tag{36}$$

where

$$\Phi(v) = \frac{1}{v_s \mathrm{ch}^2(v/v_s).} \tag{37}$$

and

$$\tilde{v} = \begin{cases} \tilde{V}_{ij} & \text{if} \quad \mathbf{r} = \mathbf{r}_{ij}, \\ 0 & \text{if} \quad \mathbf{r} \neq \mathbf{r}_{ij}, \end{cases} \tag{38}$$

In order to describe the dynamics of the considered system 50 largest LEs were calculated. For this purpose the set of 50 perturbations was obtained with the help of Gram–Schmidt procedure (step 4). Following step 5 of the algorithm, the set of Eqs. (29)–(33) and Eqs. (36)–(38) describing the dynamics of the system state and its perturbation, respectively, along with Gram–Schmidt procedure (step 6) were solved numerically to get Lyapunov exponents (step 7).

First trial was performed at the non-closed spatial configuration as sketched in the Fig. 5 *b*. Specifically, we have used Neumann boundary conditions (zero flux through the boundary) for $z(0, x)$ and $z(1, x)$. At the same time, for the upper bound $z(0, x^*)$, where $x^* \in [0.375, 0.625]$, the Dirichlet boundary conditions were used. Finally, the lateral edges $z(y, 0)$ and $z(y, 1)$ were disconnected since the k_d was set to zero. The simulations were performed on the lattice of 40×40 (i.e., $N = 40$) interacted oscillators as shown in Fig. 6.

Fig. 6, *a* demonstrates convergence of the method by presenting the dependence of selected number of LEs on time *t*. These graphs show that after $t \approx 2 \times 10^4$ (a.u) the values of the LEs almost do not change their values. With this, the presence of eighteen positive Lyapunov exponents $\lambda_1 \div \lambda_{18}$ in the spectrum (Fig. 6, *a*) reveals the

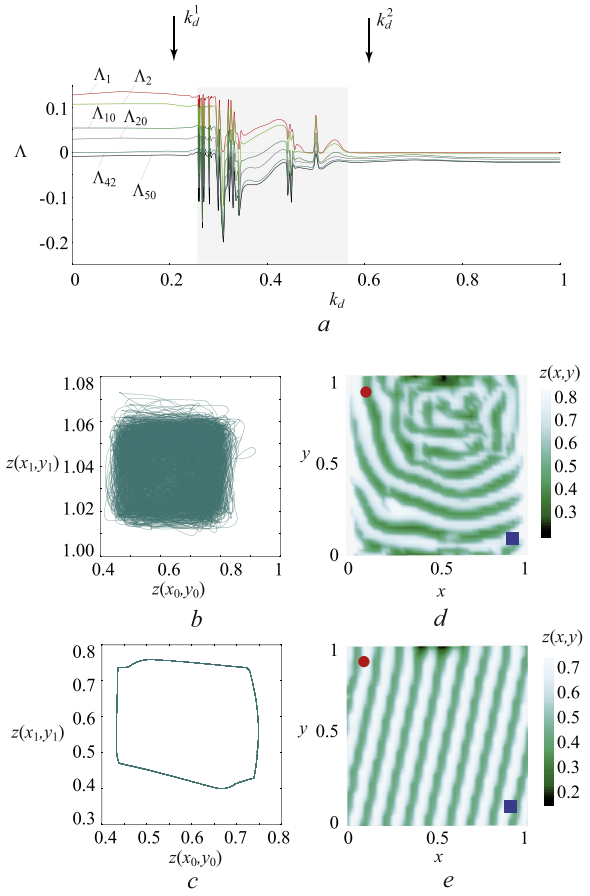

Fig. 7. The spectrum of Lyapunov exponents for the CSD model (*a*), containing the 1st, the 2nd, the 10th, the 20th, the 42nd and the 50th LEs, depending on the value of k_d, the zero-level is shown by the dashed line, the area of parameters, corresponding to the transition from the periodically spreading waves to the well-developed spatiotemporal chaos is marked by the shadow. The correlation between the evolution of the *z*-variable in the different regions of active media (namely, $z(x_1, y_1)$ and $z(x_0, y_0)$) (*b,c*) and the momentum spatial distributions $z(x, y)$ (*d,e*), corresponding to the chaotic ($k_d = k_d^1$) and periodic ($k_d = k_d^2$) regimes, respectively. The locations of the points (x_1, y_1) and (x_0, y_0) are shown by the solid circle and the solid square, the values of k_d^1 and k_d^2 are shown in (*a*) by the arrows..

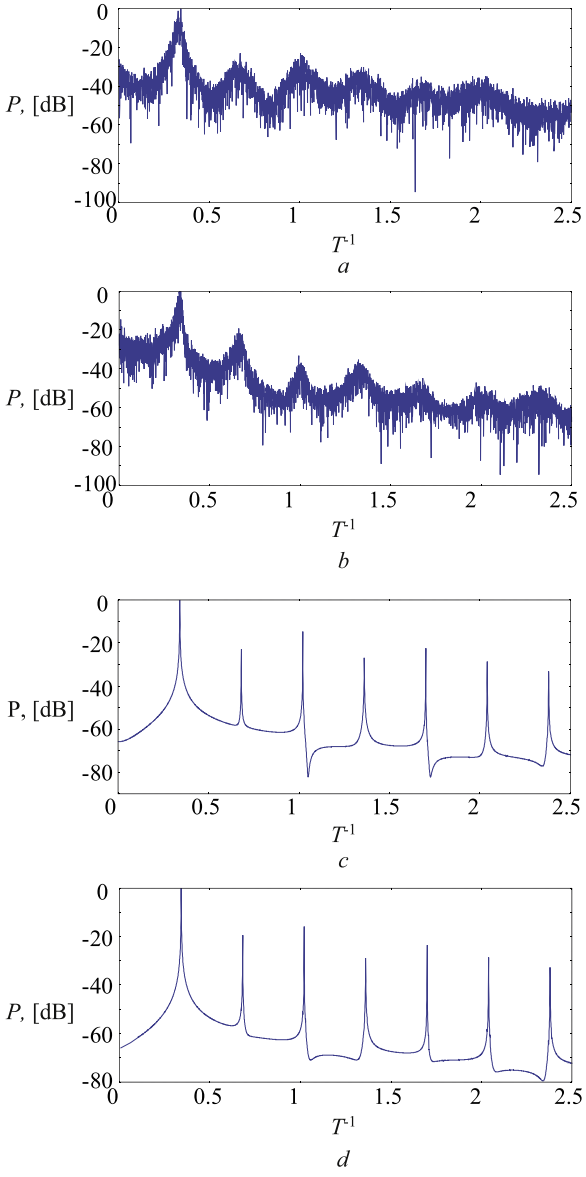

Fig. 8. Power spectra of the oscillations in two selected locations for k_d^1 and $\mathbf{r}_0 = (x_0, y_0)$ (a); for k_d^1 and $\mathbf{r}_1 = (x_1, y_1)$ (b); for k_d^2 and $\mathbf{r}_0 = (x_0, y_0)$ (c); and for k_d^2 and $\mathbf{r}_0 = (x_1, y_1)$ (d).

spatio-temporal chaos developed in this system. Indeed, as one can see from Fig. 6, *b*, the model shows the complex spatio-temporal behavior. The key feature of this chaos is the distinctive localization of the high-amplitude perturbations near the right corner of figure panels (see Fig. 6, *c,d*), exactly at the wave nucleation center that is observed in panel *b*. It confirms the hypothesis that irregular spatio-temporal pattern is generated within this area and then spreads out to occupy all the available space. During the next trial, k_d was gradually increased from zero to $k_d = 1$ in order to observe and quantify the changes in spatio-temporal dynamics caused by the evolution of modeled geometry to cylindric one as shown in Fig. 5 *a*.

In Fig. 7,*a* the selected Lyapunov exponents (from the whole spectrum) are shown, being the 1st, the 2nd, the 10th, the 20th, the 42nd and the 50th LEs, plotted against the values of $k_d \in [0, 1]$. With k_d increasing, until $k_d = k_d^1 = 0.2$ no considerable changes are observed, fully developed spatio-temporal chaos persists. For $k_d > k_d^1$ the values of all LEs behave highly irregular, showing multiple jumps between negative and positive values, except the highest one, Λ_1 which remains positive. In the k_d interval near the $k_d \approx 0.4$ there is an interesting example of smooth rise of LEs showing the gradual increase of the "degree of chaoticity". With further increase of k_d non-monotonic behavior vanishes. For $k_d > k_d^2$ two largest Lyapunov exponent are very close to zero, so one can classify this spatio-temporal dynamics as quasiperiodic one.

In Fig. 7*b–e* the representative snapshots of *z* and the cross-plot between the *z* values in two selected locations (namely, $z(x_1, y_1)$ vs $z(x_0, y_0)$) are shown for $k_d^1 = 0.2$ and $k_d^2 = 0.6$, that bound the transition area as described above. One can make sure that at k_d^1 there is the complex-shaped wave pattern (*d*) with lack of obvious correlation between two analyzed points (*b*), while on panels (*c*) and (*e*) there is the well shaped regular pattern, formed by the running waves. The corresponding power spectra of oscillations $z(\mathbf{r}, t)$ in these selected locations $\mathbf{r}_0 = (x_0, y_0)$ and $\mathbf{r}_1 = (x_1, y_1)$ are shown in Fig. 8. Fig. 8, *a,b* display the spectrum of oscillations $z(\mathbf{r}_0, t)$ and $z(\mathbf{r}_1, t)$, respectively, calculated for $k_d = k_d^1$. Both spectra are continuous and broadband, as it is typical for chaotic oscillations. For $k_d = k_d^2$, the character of the spectra dramatically changes, and for both $\mathbf{r}_0$ (Fig. 8 c) and $\mathbf{r}_1$ (Fig. 8 d) the spectra are discrete, thus evidencing of regular oscillations in the system.

Within the interval $k_d \in (0.28; 0.6)$ the Lyapunov exponents behavior reflects the multiple transitions between different regular

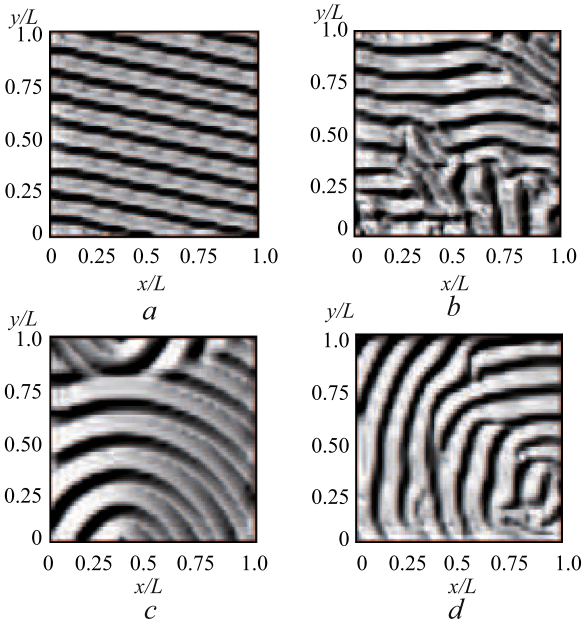

Fig. 9. The momentum spatial distributions $z(x, y)$ corresponding to the regular (a, c) and chaotic (b, d) regimes, obtained for $k_d = 0.6$ (a), $k_d = 0.5$ (b), $k_d = 0.267$ (c), $k_d = 0.261$ (d).

and irregular types of the system dynamics. Some of typical dynamical regimes observed within this range of k_d-parameter value are given in Fig. 9. When the value of k_d parameter is relatively large ($k_d \in (0.36; 0.6)$) the smooth behavior of Lyapunov exponents is mostly observed, although the transition from regular to chaotic regimes (and visa verse) takes place (see Fig. 9 *a,b*). For this types of dynamics both the regular and irregular regimes are associated with the propagation of the practically linear wave fronts. For the rather small values of k_d (namely, $k_d \in [0.26; 0.34]$) the highly irregular dependence of LEs curves on k_d-parameter takes place, with the alternating regular and irregular types of dynamics being characterized by the spiral wave propagation (see Fig. 9 *c,d*).

5. Conclusions

In conclusion, we suggest a technique to calculate the spectrum of LEs for a wide class of the dynamical systems, which are determined by set of ODEs coupled with PDEs. We have discussed an approach to introduce the reference state and its perturbations, which allows a reliable estimation of the perturbation growth/decay rate. The proposed method was applied to the two representative nonlinear DCSs with media of different dimension.

First, we considered a DCS with 1D medum, which models the charge transport in a TED connected with an external lumped RLC-circuit. The proposed method was able to unambiguously recognise the transition between regular an chaotic charge dynamics with variation of the bias voltage applied to the TED and of the resonant frequency of the RLC-circuit. These transitions were also confirmed by analysis of the spatio-temporal patterns in the charge transport along the TED as well as by calculation of the power spectral density of the current oscillations generated by the device.

Next, we tested our method by analysing the stability of dynamical patterns in DSC with 2D media describing neuron-to-neuron signalling via redistribution of ions in extracellular space. The method allowed to reveal how the changes in boundary conditions affect the regularity of the depolarization spreading. In particular, we found that the appearance of turbulent behaviour in ions redistribution within the extracellular space non-trivially depends on the penetrability of the medium boundaries. These interesting finding, supported by analysis of patio-temporal patterns and calculation of the power spectrum of the concentration oscillations, is required more thorough investigation, which is beyond the scope of the presented paper.

Generally, the developed approach bridges the gap in stability analysis of complex composite dynamical models consisting of both extended and lumped elements, and can thus be used in diverse areas of modern interdisciplinary science dealing with such systems.

Acknowledgments

This work has been supported by Russian Science Foundation (grant 14-12-00224).

References

[1] Eikenberry S. A tumor cord model for Doxorubicin delivery and dose optimization in solid tumors. Theor Biol Med Modell 2009;6:6.
[2] Soltanova KN, Prykarpatski AK, Blackmorec D. Long-time behavior of solutions and chaos in reaction-diffusion equations. Chaos, Solitons Fractals 2017;99:91–100.
[3] Eisenhofer S, Efendiev MA, Otani M, Schulz S, Zischka H. On an ODE-PDE coupling model of the mitochondrial swelling process. Discrete and Continuous Dyn Syst - SerB 2015;20(4):1031–57.
[4] Claus J, Friedmann E, Klingmuller U, Rannacher R, Szekeres T. Spatial aspects in the smad signaling pathway. J Math Biol 2013;67(5):1171–97.
[5] Postnov DE, Postnov DD, Schimansky-Geier L. Self-terminating wave patterns and self-organized pacemakers in a phenomenological model of spreading depression. Brain Res 2012;1434:200–11.
[6] Andersen UL, Neergaard-Nielsen JS, van Loock P, Furusawa A. Hybrid discrete- and continuous-variable quantum information. Nat Phys 2015;11:713–19.
[7] Hramov AE, Koronovskii AA, Kurkin SA, Makarov VV, Gaifullin MB, Alekseev KN, et al. Subterahertz chaos generation by coupling a superlattice to a linear resonator. Phys Rev Lett 2014;112:116603.
[8] Daafouz J, Tucsnak M, Valein J. Nonlinear control of a coupled PDE/ODE system modeling a switched power converter with a transmission line. Syst Control Lett 2014;70:92–9.
[9] Schwartz IB, Morgan DS, Billings L, Lai Y-C. Multi-scale continuum mechanics: from global bifurcations to noise induced high-dimensional chaos. Chaos 2004;14(2):373–86.
[10] Gabe IT. Arterial blood flow by analogue solution of the Navier-Stokes equation. Phys Med Biol 1965;10(2):271–80.
[11] DeVault K, Gremaud PA, Novak V, Olufsen MS, Vernieres G, Zhao P. Blood flow in the circle of willis: modeling and calibration. Multiscale Model Simul 2008;7(2):888–909.
[12] Lo W-C, Zheng L, Nie Q. A hybrid continuous-discrete method for stochastic reaction diffusion processes. R Soc Open Sci 2016;3(9):160485.
[13] Postnov DE, Chetverikov AP, Postnov DD. Stimulus-induced response patterns of medium-embedded neurons. Eur Phys J Spec Top 2010;187:241–53. doi:10.1140/epjst/e2010-01289-8.
[14] Berthier F, Diard J-P, Montella C. Numerical solution of coupled systems of ordinary and partial differential equations. application to the study of electrochemical insertion reactions by linear sweep voltammetry. J Electroanal Chem 2001;502:126–31.
[15] García S, niguez-de-la Torre II, Pérez S, Mateos J, González T. Numerical study of sub-millimeter Gunn oscillations in InP and GaN vertical diodes: dependence on bias, doping, and length. J Appl Phys 2013;114:074503.
[16] Yurchenko VB, Yurchenko LV. Bistability and hysteresis in the emergence of pulses in microstrip Gunn-diode circuits. AIP Adv 2014;4:127126.
[17] Shiau Y-H, Cheng Y-C. Hybrid electric-field domains leading to spatiotemporal chaos in n-GaAs. Phys Rev B 1997;56(15):9248.
[18] Zhou L, Chen Z, Wang Z, Wang J. On the analysis of local bifurcation and topological horseshoe of a new 4D hyper-chaotic system. Chaos, Solitons Fractals 2016;91:148–56.
[19] Singh JP, Roy BK. The nature of Lyapunov exponents is (+, +, ,). is it a hyper-chaotic system? Chaos, Solitons Fractals 2016;92:73–85.
[20] Zamanie N, Ataei M, Niroomand M. Analysis and control of chaotic behavior in boost converter by ramp compensation based on Lyapunov exponents assignment: theoretical and experimental investigation. Chaos, Solitons Fractals 2015;81:20–9.
[21] Li Z, Sun S, Huang Y. Exploring inventory order policies impact under the non-negative constraint of order quantity: system stability, service level, and cost,. Chaos, Solitons Fractals 2017;103:111–22.
[22] Hramov AE, Koronovskii AA, Kurovskaya MK, Moskalenko OI. Analytical expression for zero Lyapunov exponent of chaotic noised oscillators,. Chaos, Solitons Fractals 2015;78:118–23.
[23] Gomez IS. Lyapunov exponents and poles in a non Hermitian dynamics,. Chaos, Solitons Fractals 2017;99:155–61.
[24] Upadhyay RK, Mondal A. Synchronization of bursting neurons with a slowly varying d. c. current,. Chaos, Solitons Fractals 2017;99:195–208.

[25] Kuptsov PV. Computation of Lyapunov exponents for spatially extended systems: advantages and limitations of various numerical methods. Appl Nonlinear Dyn 2010;18(5):80–92.
[26] Yang HL, Radons G. Lyapunov modes in extended systems. Phil Trans R Soc A 2009;367:3197–212.
[27] Koronovskii AA, Hramov AE, Maximenko VA, Moskalenko OI, Alekseev KN, Greenaway MT, et al. Lyapunov stability of charge transport in miniband semiconductor superlattices. Phys Rev B 2013;88:165304.
[28] Hramov AE, Koronovskii AA, Maximenko VA, Moskalenko OI. Computation of the spectrum of spatial Lyapunov exponents for the spatially extended beam–plasma systems and electron-wave devices. Phys Plasmas 2012;19(8):082302.
[29] Filatova AE, Hramov AE, Koronovskii AA, Boccaletti S. Synchronization in networks of spatially extended systems. Chaos 2008;18(2):023133. doi:10.1063/1.2940685.
[30] Moskalenko OI, Phrolov NS, Koronovskii AA, Hramov AE. Synchronization in the network of chaotic microwave oscillators. Eur Phys J Spec Top 2013;222:2571–82.
[31] Benettin G, Galgani L, Giorgilli A, Strelcyn J-M. Lyapunov characteristic exponents for smooth dynamical systems and for Hamiltonian systems: a method for computing all of them. P. I. Theory. P. II. Numerical application. Meccanica 1980;15:9–30.
[32] Wolf A, Swift J, Swinney HL, Vastano J. Determining Lyapunov exponents from a time series. Physica D 1985;16:285.
[33] Matsumoto H, Yokoyama H, Summers D. Computer simulations of the chaotic dynamics of the Pierce beam–plasma system. Phys Plasmas 1996;3(1):177.
[34] Finn JM, del Castillo-Negrete D, Barnes DC. Destabilization of the m = 1 diocotron mode in non-neutral plasmas. Phys Rev Lett 2000;84(11):2401–4.
[35] Klinger T, Schroder C, Block D, Greiner F, Piel A, Bonhomme G, et al. Chaos control and taming of turbulence in plasma devices. Phys Plasmas 2001;8(5):1961–8.
[36] Hramov AE, Koronovskii AA, Rempen IS. Controlling chaos in spatially extended beam-plasma system by the continuous delayed feedback. Chaos 2006;16(1):013123.
[37] Amann A, Schlesner J, Wacker A, Schöll E. Chaotic front dynamics in semiconductor superlattices. Phys Rev B 2002;65(19):193313.
[38] Greenaway MT, Balanov AG, Schöll E, Fromhold TM. Controlling and enhancing terahertz collective electron dynamics in superlattices by chaos-assisted miniband transport. Phys Rev B 2009;80:205318.
[39] Brondijk JJ, Spijkman M, van Seijen F, Blom PW, de Leeuw DM. Formation of inversion layers in organic field-effect transistors. Phys Rev B 2012;85(16):165310.
[40] Godfrey BB. Oscillatory nonlinear electron flow in Pierce diode. Phys Fluids 1987;30:1553.
[41] Klinger T, Latten A, Piel A, Bonhomme E, Pierre T. Chaos and turbulence studies in low–β plasmas. Plasma Phys Control Fusion 1997;39:145.
[42] Madon A, Klinger T. A model for the bifurcations in plasma drift–waves. Physica D 1997;102:355.
[43] Hramov AE, Rempen IS. Investigation of the complex dynamics and regime control in Pierce diode with the delay feedback. Int J Electron 2004;91:1. A. Madon, T. Klinger, A model for the bifurcations in plasma drift–waves, Physica D 102 (1997) 355
[44] Esaki L, Tsu R. Superlattices and negative differential conductivity in semiconductors. IBM J Res Dev 1970;14(1):61–5.
[45] Shik AY. Superlattices-periodic semiconductor structures. Sov Phys Semicond 1975;8:1195.
[46] Wacker A. Semiconductor superlattices: a model system for nonlinear transport. Phys Rep 2002;357:1–111.
[47] Fromhold TM, Patane A, Bujkiewicz S, Wilkinson PB, Fowler D, Sherwood D, et al. Chaotic electron diffusion through stochastic webs enhances current flow in superlattices. Nature 2004;428:726–30.
[48] Alexeeva N, Greenaway MT, Balanov AG, Makarovsky O, Patane A, Gaifullin MB, et al. Controlling high-frequency collective electron dynamics via single-particle complexity. Phys Rev Lett 2012;109(2):024102.
[49] Hramov AE, Makarov VV, Maksimenko VA, Koronovskii AA, Balanov AG. Intermittency route to chaos and broadband high-frequency generation in semiconductor superlattice coupled to external resonator. Phys Rev E 2015;92:022911.
[50] Li W, Reidler I, Aviad Y, Huang Y, Song H, Zhang Y, et al. Fast physical random-number generation based on room-temperature chaotic oscillations in weakly coupled superlattices. Phys Rev Lett 2013;111:044102.
[51] Charles AC, Baca SM. Cortical spreading depression and migraine. Nat Rev Neurol 2013;9(11):637–44.
[52] Tfelt-Hansen PC. History of migraine with aura and cortical spreading depression from 1941 and onwards. Cephalalgia 2010;30(7):780–92.
[53] Heiss WD. The ischemic penumbra: how does tissue injury evolve? Ann N Y Acad Sci 2012;1268:26–34.
[54] Agnati L, Zoli M, Strömberg I, Fuxe K. Intercellular communication in the brain: wiring versus volume transmission. Neuroscience 1995;69(3):711–26.
[55] Postnov DE, Muller F, Schuppner RB, Schimansky-Geier L. Dynamical structures in binary media of potassium-driven neurons. Phys Rev E 2009;80(3 Pt 1):031921.